Alternative Splicing at N Terminus and Domain I Modulates Ca$_V$1.2 Inactivation and Surface Expression

Peter Bartels,[1] Dejie Yu,[1] Hua Huang,[1] Zhenyu Hu,[1] Stefan Herzig,[2] and Tuck Wah Soong[1,3,4,5,*]

[1]Department of Physiology, National University of Singapore, Singapore, Singapore; [2]Department of Pharmacology, University of Cologne, Cologne, Germany; [3]NUS Graduate School for Integrative Sciences and Engineering and [4]Neurobiology/Ageing Programme, National University of Singapore, Singapore, Singapore; and [5]National Neuroscience Institute, Singapore, Singapore

ABSTRACT The Ca$_V$1.2 L-type calcium channel is a key conduit for Ca^{2+} influx to initiate excitation-contraction coupling for contraction of the heart and vasoconstriction of the arteries and for altering membrane excitability in neurons. Its α_{1C} pore-forming subunit is known to undergo extensive alternative splicing to produce many Ca$_V$1.2 isoforms that differ in their electrophysiological and pharmacological properties. Here, we examined the structure-function relationship of human Ca$_V$1.2 with respect to the inclusion or exclusion of mutually exclusive exons of the N-terminus exons 1/1a and IS6 segment exons 8/8a. These exons showed tissue selectivity in their expression patterns: heart variant 1a/8a, one smooth-muscle variant 1/8, and a brain isoform 1/8a. Overall, the 1/8a, when coexpressed with Ca$_V\beta_{2a}$, displayed a significant and distinct shift in voltage-dependent activation and inactivation and inactivation kinetics as compared to the other three splice variants. Further analysis showed a clear additive effect of the hyperpolarization shift in $V_{1/2inact}$ of Ca$_V$1.2 channels containing exon 1 in combination with 8a. However, this additive effect was less distinct for $V_{1/2act}$. However, the measured effects were β-subunit-dependent when comparing Ca$_V\beta_{2a}$ with Ca$_V\beta_3$ coexpression. Notably, calcium-dependent inactivation mediated by local Ca^{2+}-sensing via the N-lobe of calmodulin was significantly enhanced in exon-1-containing Ca$_V$1.2 as compared to exon-1a-containing Ca$_V$1.2 channels. At the cellular level, the current densities of the 1/8a or 1/8 variants were significantly larger than the 1a/8a and 1a/8 variants when coexpressed either with Ca$_V\beta_{2a}$ or Ca$_V\beta_3$ subunit. This finding correlated well with a higher channel surface expression for the exon 1-Ca$_V$1.2 isoform that we quantified by protein surface-expression levels or by gating currents. Our data also provided a deeper molecular understanding of the altered biophysical properties of alternatively spliced human Ca$_V$1.2 channels by directly comparing unitary single-channel events with macroscopic whole-cell currents.

INTRODUCTION

Voltage-gated Ca^{2+} channels play a pivotal role in excitable cells, where they transduce electrical signals into a large spectrum of cardiovascular and neurophysiological functions such as excitation-contraction coupling in muscles, hormone secretion in endocrine cells, and excitation-transcription coupling in neurons (1–8). The functional Ca$_V$1.2 channel is a heteromultimeric protein complex consisting of the pore-forming α_{1C} submit in association with the $\alpha_2\delta$ and the β subunits. The auxiliary subunits regulate surface membrane expression and channel kinetics (9–12). The inactivation of Ca$_V$1.2 calcium channels is a dynamic and fast (milliseconds) intrinsic regulatory process, composed of voltage and time-dependent components, that

serves to tightly control the amount of Ca^{2+} entering a cell during membrane depolarization. Apart from this intrinsic nature of the Ca$_V$1.2 channel to activate and inactivate upon sensing membrane depolarization, alternative splicing can modify channel properties and fine-tune Ca^{2+} entry to affect membrane excitability (13,14). Altered or derailed regulation of the splicing machinery of the Ca$_V$1.2 subunit has been shown to result in severe phenotypes with life-threatening cardiovascular disorders (15–17). To date, it has been reported that at least 20 out of 56 exons encoding the human Ca$_V$1.2 channel undergo alternative splicing (18–24). However, the biological and phenotypic consequences attributed to each alternative splicing event are not well understood. In previous works by our group and others, we have demonstrated the diversification of Ca$_V$1.2 pharmacological and electrophysiological properties by alternative splicing and have related their relevance and importance to vasotone and cardiac arrhythmia

(21,25–29). Recently, we reported for the first time the severe in vivo consequences of the altered $Ca_V1.2$ channel biophysical property arising from the exclusion of cassette exon 33 and suggested its role in the pathomechanism of human heart failure (14). In this report, we aimed to evaluate the functional consequences underlying alternative splicing within the N-terminus and domain I of the human $Ca_V1.2$ calcium channel. It has been shown that alternative splicing at exon 1 of the N-terminus of $Ca_V1.2$ affects channel regulation and its surface expression (30–33). On the other hand, there exists tissue-selective distribution of $Ca_V1.2$ transcripts of the predominant heart 1a/8a and one smooth-muscle 1/8 isoform (19). To date, combinations of 1a/8a, 1a/8, 1/8a, and 1/8 have been described, but they have neither been characterized together nor by single-channel recordings for careful analysis (24).

Here, we report that voltage-dependent inactivation, inactivation kinetics, membrane surface expression, and local Ca^{2+}-sensing calmodulin (CaM) N-lobe regulation of $Ca_V1.2$ channels are influenced by the N-terminus and domain I composition, with particular attention focused on exons 1/1a and exons 8/8a. By using an electrophysiological approach and a direct comparison of micro- and macrocurrents, the 1/8a-$Ca_V1.2$ isoform was characterized to display a clearly distinguishable inactivation kinetic that is more accelerated as compared to the 1a/8a splice variant. These results suggest that both the N-terminus and IS6 have a different impact on voltage and/or inactivation kinetics. Although exon 1a produced modest NSCaTE (34) effects involving local Ca^{2+}-sensing by the N-lobe of CaM (N-lobe calcium-dependent inactivation (CDI)), exon 1 modulates N-lobe CDI to a larger extent (f_{300} at 0 mV) as it was more enhanced. Overall, exon-1-containing $Ca_V1.2$ channels displayed significantly larger Ba^{2+} and Ca^{2+} currents, which correlated well with a higher channel surface expression that we quantified by a biotinylation approach and by examining voltage segment movements (Q_{on}). A direct comparison of all isoforms showed a much larger ion movement across the cell surface membrane upon depolarization for the exon-1-containing $Ca_V1.2$ channels, whereas the single-channel gating properties remained unaltered. Our data reveal interesting and unexpected information about $Ca_V1.2$ channel gating kinetics underlain by alternative splicing of the N-terminus and domain I.

MATERIALS AND METHODS

Generation of cardiac- and brain-specific $Ca_V1.2$ calcium channel isoforms

The various human splice variants we generated from the reference clone 77WT isoform (1/8/Δ9*/22/32) that was kindly provided by Dr. Roger Zühlke. For subclonings, 77WT was digested with *Xba* I and *Afe* I, and the respective fragments containing 1a/8a, 1/8a, and 1a/8 were substituted into 77WT. All constructs were verified by DNA sequencing.

Cell culture and transient transfection

HEK 293 cells were transiently transfected with equimolar amounts (1.5 μg cDNA) of α_{1c} isoforms, rat β_{2a} or β_3, and $\alpha_2\delta_1$ (kind gifts of Dr. Terry P. Snutch, UBC, Canada) and 0.25 μg T-antigen plasmid using the calcium phosphate method. For NSCaTE CDI experiments, 1 μg of $CaM_{3,4}$ was additionally co-transfected. Cells were then incubated at 37°C, 5% CO_2 for 48–72 h before patch-clamp electrophysiological experiments were performed.

Whole-cell patch-clamp recordings

Ba^{2+} currents (I_{Ba}) of human $Ca_V1.2$ isoforms were recorded from transiently transfected HEK 293 cells in the whole-cell or cell-attached configuration. For whole-cell recordings, the external solution contained (in mM): 140 tetraethylammonium methanesulfonate (TEA), 10 HEPES, 5 $BaCl_2$ or 5 $CaCl_2$ with a pH adjusted to 7.4 (CsOH), and an osmolarity of 310–330 (Glucose). The internal pipette solution contained (in mM): 138 Cs-MeSO$_3$, 5 CsCl, 0.5 EGTA, 1 $MgCl_2$, 10 HEPES, and 2 mg/mL Mg-ATP, pH adjusted to 7.3 (CsOH), milliosmole 290–330 (Glucose). For NSCaTE CDI experiments, 0.5 mM EGTA or 10 mM BAPTA (A4926; Sigma-Aldrich, St. Louis, MO) was used in the internal pipette solution. Pipette resistance of borosilicate pipettes was usually 1.5–2.5 MΩ. The series resistance (usually <8 MΩ) and the cell capacitance was directly taken from a MultiClamp 700B Amplifier (Molecular Device, San Jose, CA) and compensated to its maximal extension (~70%) to avoid current oscillation. Barium currents were sampled at 10 kHz and low-pass-filtered at 1 kHz. Raw data acquisition was obtained with pClamp 10 and stored in a common CPU. Data analysis and curve fitting were performed by using GraphPad Prism IV software (San Diego, CA). The current-voltage (I-V) relationship was obtained from a holding potential (HP) of −100 mV and pulsed for 900 ms to various testing potentials (TP) starting from −60 to +50 mV (Δ10 mV increments). The elicited currents (I_{Ba}) were then normalized over all TP to its peak maximal currents. The I-V relationship was fitted with a modified Boltzmann, respectively:

$$I = G_{max} \times \frac{(V - E_{rev})}{1 + \exp[(V - V_{0.5})/k_{act}]}, \qquad (1)$$

where G_{max} is the maximal slope conductance, E_{rev} is the reverse potential, $V_{0.5}$ is the half-maximal activated potential, and k is the slope factor. The steady-state inactivation was obtained from an HP of −100 mV stepping to a normalizing pulse of 10 mV for 30 ms, followed by a series of 15 s. Prepulses went from −120 to 20 mV. Finally, a 104-ms-long test pulse to +10 mV was recorded. Data were fitted with a single Boltzmann, respectively:

$$I = I_{min} + \frac{(I_{max} - I_{min})}{1 + exp[(V_{0.5} - V)/k_{inact}]}, \qquad (2)$$

where I is the normalized current, I_{min} and I_{max} are the current extremes, and $V_{0.5}$ is the half-maximal inactivation. The steady-state activation kinetics was determined by tail currents, in which cells were depolarized by a 20-ms test pulse of a series of activating potentials starting from −60 to +120 mV. Tails were then measured after repolarization to −50 mV for 10 ms, and the normalized currents were fitted with a dual Boltzmann function, respectively:

$$\frac{G}{G_{max}} = \frac{F_{low}}{1 + \exp[(V_{0.5,low} - V)/k_{low}]} + \frac{1 - F_{low}}{1 + \exp[(V_{0.5,high} - V)/k_{high}]}, \qquad (3)$$

with G as the tail current and G_{max} as the peak tail current. F_{low} is the fraction of the low-threshold component; $V_{0.5,low}$, $V_{0.5,high}$, k_{low}, and k_{high} are the half-activation potentials and slope factors for the low and high threshold components; and $V_{1/2act}$ was determined when $G = 0.5G_{max}$. Whole-cell data were leak- and capacity-corrected with an online *P/4* protocol. The liquid junction potential was not corrected in the experiment.

Cell-attached patch-clamp recordings were recorded using an Axopatch 200B amplifier (Axon Instruments, Foster City, CA). Data were filtered at 2 kHz (-3 dB, four-pole Bessel) and sampled at 10 kHz. Cells were depolarized (in mM) with 110 BaCl$_2$ and 10 mM HEPES (pH 7.4) (TEA-OH) for 150 ms from an HP of -100 mV to its maximal resolvable TP of usually $+10$ mV. Pulse frequency was 1 kHz to fully allow for recovery of the channels in the patch. To collapse the membrane potential, a potassium-rich bath solution was used containing (in mM): 120 K-glutamate, 25 KCl, 2 MgCl$_2$, 10 HEPES, 2 EGTA, 1 CaCl$_2$, 1 Na2-ATP, and 10 dextrose (pH 7.4) (KOH). Thermal noise was reduced by heavy elastomeric-coated pipettes (borosilicate glass, 6–7 MΩ) using Sylgard 184 (Dow Corning, Midland, MI). The pClamp10 software package was used for data acquisition and analysis. All experiments were carried out at room temperature (21–23°C). Raw data single-channel events were detected using the half-height criterion (35) and digitally leak- and capacity-corrected. The filter rise time (t_r) of our system was calculated to approximately at 166 μs, based on $t_r = 0.3321/f_c$, where f_c represents the cutoff frequency at 2 kHz. Consequently, events <166 μs were not considered as channel events, as they were more likely to be of systemic artificial origin. The number of channels in the patch was estimated by the occurring number of staged openings recorded over several minutes at depolarizing TP. Usually patches with more than three channels were not considered for statistical analysis because of an overinterpretation of channel open probability (P_{open}). Channel correction and number were adopted from previous publications (36,37). For a sufficient statistical analysis, a minimum of 180 traces was recorded for each experiment. The mean ensemble average current was derived from 180 idealized traces, whereas the local maximum (I_{peak}) was estimated by using a simple smoothening algorithm (fast Fourier transform) to abolish high-frequency noise. The fraction of active sweeps (availability) was calculated by the number of active traces (M_{active}) divided by the total number of sweeps (M_0). Dwell-time histogram binning was performed according to Sigworth and Sine (38) and fitted with a mean simplex method.

Surface protein biotinylation assay

For surface biotinylation of Ca$_V$1.2 channels transfected into HEK 293 cells, Ca$_V$1.2 proteins were biotinylated using an EZ-Link Sulfo-NHS-Biotinylation Kit (Thermo Fisher Scientific, Waltham, MA). Briefly, cells were incubated with 0.5 mg/mL biotin for 1 h at 4°C. Unbound biotin was removed in quenching buffer by incubating for 20 min, and the proteins were washed with phosphate-buffered saline buffer. After the measurement of protein concentration, NeutrAvidin (Pierce, Appleton, WI) was used to pull down the biotinylated surface proteins by incubating with cell lysates overnight. Avidin-bound proteins were eluted by boiling in 2× sample loading buffer and then loaded on SDS-PAGE gel.

Statistics

Data are given as pooled data with their mean values with standard error, respectively (mean ± SE). Statistical comparison of several groups was performed by a one-way analysis of variance (ANOVA) and subsequent Bonferroni correction if not stated otherwise. Additionally, an unpaired t-test was performed to compare partner groups. Data were considered as statistically significant based on a 95% confidence interval.

RESULTS

Whole-cell electrophysiological recordings of N-terminal alternatively spliced Ca$_V$1.2 isoforms revealed changes in current density and channel kinetics

The expression of the human heart Ca$_V$1.2 isoform has been described to be regulated by a distinct 5′ regulatory element employing a promoter for tissue-specific expression (39,40). The N-terminal exon 1 can be alternatively spliced by utilizing alternative 5′ promoters to produce exon 1a, which is predominantly expressed in cardiac muscle cells; exon 1, which is predominantly expressed in smooth muscle cells; or exon 1c, which is highly expressed in resistance and cerebral arteries (26,31,32,41). We and others have elucidated the presence of multiple splice variants in rats and rabbits, and these variants showed distinct electrophysiological and pharmacological properties and modulatory sites (19,20,24,42,43). Notably, exon 1c is mainly expressed in arterial myocytes and to a lesser extent in cardiac myocytes (31). By using the traditionally known and narrowly defined cardiac-muscle- (exons 1a/8a) specific and one smooth-muscle- (exons 1/8) specific Ca$_V$1.2 isoforms (25), which differ only in the N-terminus and domain 1, we have characterized their macroscopic and microscopic currents. To fully characterize the four permutations of exons 1/1a in combination with mutually exclusive exons 8/8a, we generated the two other constructs containing either 1a/8 or 1/8a of Ca$_V$1.2 by simply substituting them into the reference 77WT clone that Zühlke et al. (44) reported (Fig. 1, A–C). The brain 1/8a splice variant was isolated in rats, but the predominant combinatorial splicing pattern in the brain is less well defined (45). To determine the I-V, the splice variants, with Ca$_V\beta_{2a}$ and Ca$_V\alpha_2\delta_1$, transfected into HEK 293 cells were depolarized for 900 ms from a HP of -100 mV to various TP (starting from -60 to $+50$ mV, $\Delta10$ mV increments). Representative current traces of comparable cell size (Fig. 2 A) showed larger maximal I_{Ba} that appeared to be three- to fourfold larger for the 1/8a isoform in comparison to all other isoforms. The currents, obtained after fitting with a Boltzmann-Ohm function (Eq. 1), indicate a potential change in activation/inactivation kinetics, of which the 1/8a was most pronounced (Fig. 2 B). In corroboration, the half-maximal activation potential ($V_{1/2}$) for 1/8a was shifted by up to -5.0 mV to more hyperpolarized potential, which is significantly more negative as compared to the isoforms 1a/8a, 1/8, and 1a/8 (Fig. 2 B; Table 1). Furthermore, an obvious increase in current density, which was observed over a range of depolarizing TP, could be detected for the exon 1 isoform (Fig. 2 C; Table 1). On average, the current density of the 1/8a isoform was increased with a maximal conductance (G_{max}) of more than 100% as compared to the 1a/8a isoform. To further test for relevance in the smooth muscle context, we performed experiments coexpressing the isoforms with the smooth-muscle-expressing β_3-subunit instead of the previously used β_{2a}-subunit (Fig. S1, A–C; Table S1). Overall, the data clearly indicate that the exon-1-containing isoforms have bigger current densities as compared to exon-1a-containing splice variants and that this effect is β-subunit independent. These results suggest that higher channel surface expression could be associated with channels expressing the shorter N-terminal exon 1.
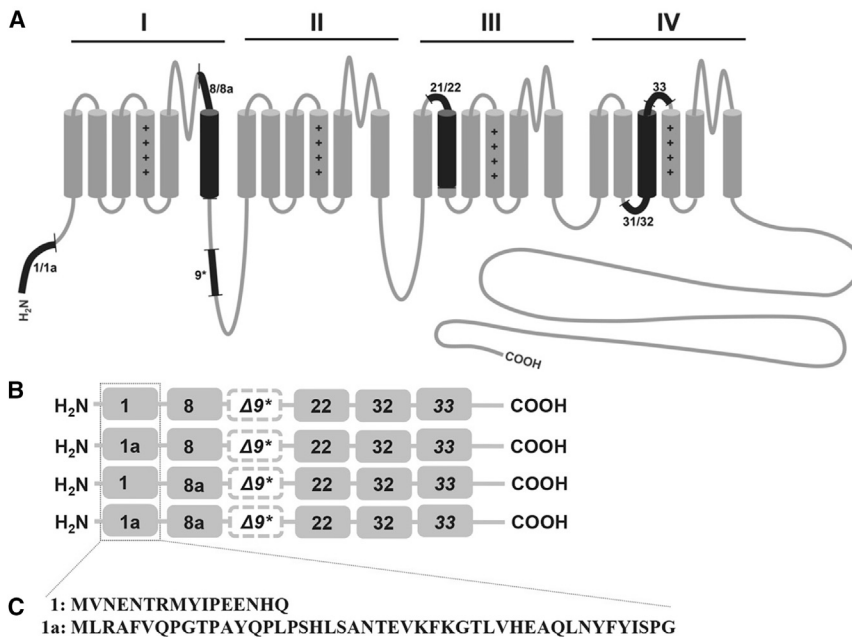
FIGURE 1 (*A*) Topology of the Ca$_V$1.2 channel structure with the four transmembrane spanning domains I-IV. Relevant alternative splicing sites are highlighted in black. (*B*) A schematic representation of the splicing profile of Ca$_V$1.2 isoforms 1/8, 1a/8, 1/8a, and 1a/8a is shown. (*C*) The amino acid alignment of the long-form exon 1a and the short-form exon 1 of Ca$_V$1.2 is given.

We further examined the steady-state inactivation property of the various isoforms and found that the 1/8a showed faster voltage-dependent inactivation during depolarization to maximal V_{max} than 1a/8a (Fig. 3 *A*, *left*), and the percentage of Ba^{2+} inward currents was significantly reduced at 0.3, 0.6, and 0.9 s pulses to V_{max} by more than 40% (Fig. 3 *C*, *left*). However, this trend was not observed when comparing 1/8 with 1a/8 isoforms (Fig. 3, *A* and *C*, *right*). This demonstrates that voltage-dependent inactivation is primarily determined by the shorter exon 1 as compared to 1a and in the context of 8a. However, exons 8/8a coding for domain IS6 seemed to be additionally involved in the modulation of channel inactivation, with 8a producing a larger amount in inactivation. We then evaluated the time course of inactivation (τ-values) that we obtained from monoexponential fits. The τ-values for the isoforms containing exons 1/8a and 1a/8a were significantly faster at 0 mV as compared to 1a/8 and 1/8 (Fig. 3 *B*, two-way ANOVA, Tukey's multiple comparison, ***$p < 0.001$ and **$p < 0.001$). The faster time course in channel inactivation clearly determines the involvement of segment IS6 in Ca$_V$1.2 channel inactivation.

Local Ca^{2+}-sensing N-lobe regulation of Ca$_V$1.2 by CaM is modulated by exon 1 alternative splicing

Global and local Ca^{2+} levels within a cell have been described to be selectively sensed through a distinct mechanism involving the N- and C-lobes of Ca^{2+}/CaM-modulating Ca$_V$ calcium channels (46–48). Additionally, N-terminal spatial Ca^{2+} selectivity has been reported to undergo modulation via the N-lobe of CaM and the N-terminal spatial Ca^{2+} transforming element (NSCaTE) of L-type Ca$_V$1.2 and Ca$_V$1.3 calcium channels (34).

To examine whether alternative splicing of exon 1 may affect N-lobe CDI, we co-transfected CaM$_{34}$, in which the two C-lobe EF hands are mutated, with the various Ca$_V$1.2 splice variants and performed whole-cell recordings in either 0.5 mM EGTA or 10 mM BAPTA. Here, we report that N-lobe CDI was manifested by a stronger accelerated decay of I_{Ca} against I_{Ba} currents for the 1/8a isoform (Fig. 4 *C*) over the 1a/8a isoform (Fig. 4 *A*) in 0.5 mM EGTA, whereas in 10 mM BAPTA, there was no significant difference (Fig. 4, *B* and *D*). Although global Ca^{2+} buffering by 0.5 mM EGTA resulted in significantly more robust CDI for the 1/8a splice variant as compared to the 1a/8a variant, in local Ca^{2+} buffering conditions (10 mM BAPTA) the effect was not significantly different (Fig. 4 *E*, unpaired *t*-test ***$p < 0.001$, 0 mV).

Overall, the data showed that although exon 1a supports a modest N-lobe CDI, the inclusion of exon 1 produces more than a 70% increase in CDI triggered by local Ca^{2+}-sensing by the N-lobe.

Ca$_V$1.2 channel inactivation and activation kinetics are influenced by the N-terminus and IS6 segment

To further determine the changes in biophysical gating properties, we analyzed the kinetics of inactivation and activation under steady-state conditions (Figs. 5 and 6). To examine Ca$_V$1.2 channel inactivation kinetics, HEK 293 cells were held for 15 s at various potentials, a short test pulse before and after the prepulse was recorded, and the remaining currents were normalized to
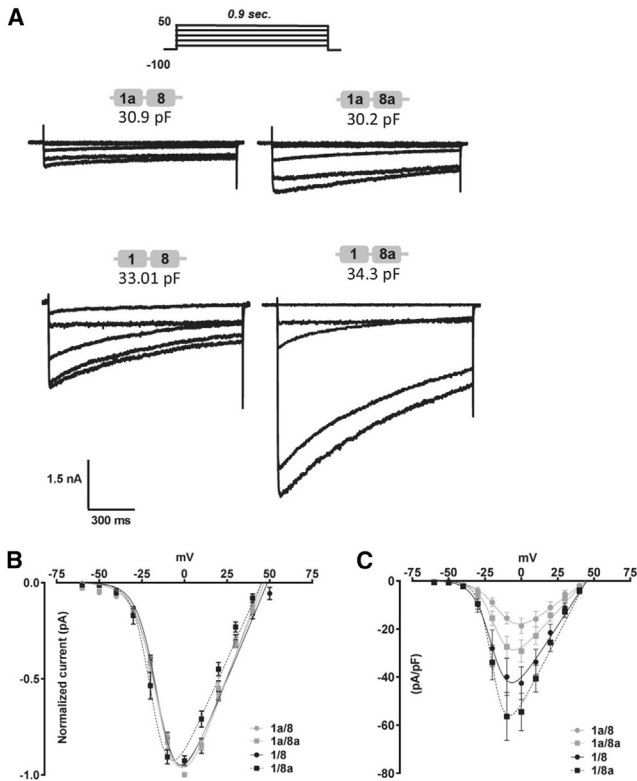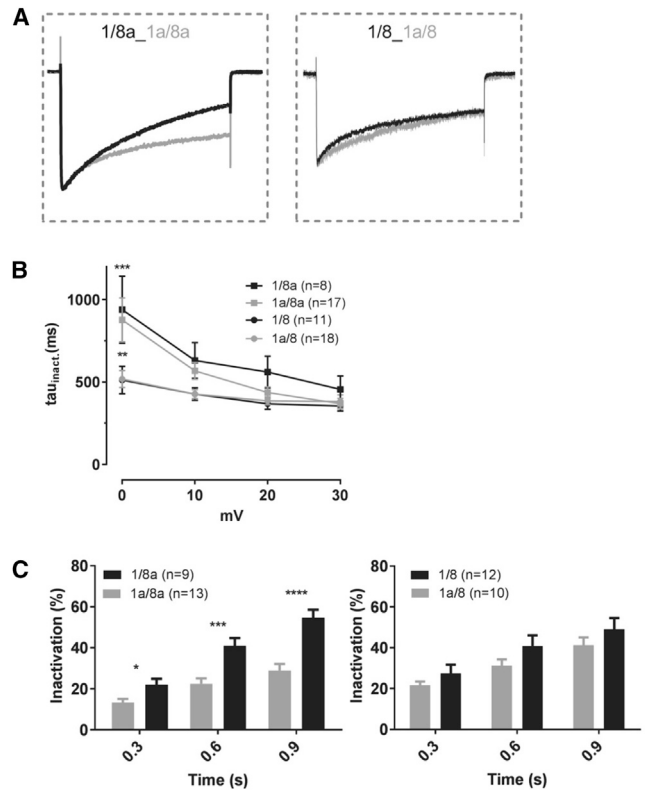
FIGURE 2 Current-voltage (I-V) relationships of N-terminal-spliced Ca$_V$1.2 isoforms determined by electrophysiological recordings in 5-mM Ba^{2+}. (A) Representative current traces recorded at a holding potential (HP) of −100 mV and stepped to various depolarizing test potentials (TPs) of −60, −30, −10, 0, and 30 mV are shown. (B) An ensemble of normalized I-V relationships of N-terminal-spliced isoforms is shown. The I-V relationships were fitted with a modified Boltzmann-Ohm function. Currents were elicited over various TPs for 900 ms. (C) The current densities were normalized to the cell capacitance (pA/pF). The number of recorded cells and kinetic constants are tabulated in Table 1.

FIGURE 3 Inactivation kinetics of Ca$_V$1.2 isoforms. (A) A comparison of superimposed traces normalized to the maximal current for 1/8a_1a/8a (left) and 1/8_1a/8 (right) is shown. (B) The voltage-dependent inactivation (Tau inactivation values) was determined with a monoexponential fit at TP of 0, 10, 20, and 30 mV. (C) The percentage of channel inactivation was determined at time points 0.3, 0.6, and 0.9 s. The statistical significance was determined by a Student's t-test (B), *$p < 0.01$, **$p < 0.001$, and ****$p < 0.0001$, and (C), statistical significance among groups for each TP was obtained by a two-way ANOVA, followed by a Tukey's multiple comparisons test, ***$p < 0.001$, **$p < 0.01$, and n = 8–18 cells.

the initial current (Fig. 5 A). The half-maximal inactivation ($V_{1/2inact}$) of 1/8a was shifted by more than −10 mV to more hyperpolarized potentials (Fig. 5 B; *$p < 0.05$, one-way ANOVA, Table 2), whereas the half-maximal activation ($V_{1/2act.}$) kinetics only changed marginally but significantly by −2 mV (Fig. 6, A and B, one-way ANOVA, *$p < 0.05$, Table 3). Overall, the slope factors remained similar for steady-state inactivation and the lower component of GV curves (K_{low}) across all four

isoforms. On the higher component (K_{high}), a much larger discrepancy in slope was observed and at the same time with a much bigger standard error. Besides Ca$_V\beta_{2a}$, we also tested Ca$_V\beta_3$ to evaluate changes in the biophysical properties of the Ca$_V$1.2 splice variants for relevance of their functions in smooth muscle and brain tissues (32). In a direct comparison of kinetic activation and inactivation, parameters were affected, although to a much weaker

TABLE 1 I-V Relationship of Ca$_V$1.2 Isoforms in 5 mM Ba^{2+}

Parameters/Splice Isoform	$V_{1/2}$ (mV)	k	E_{rev} (mV)	n	G_{max} (pA/pF)	n
1a/8	−12.9 ± 0.5[a]	−7.0 ± 0.3	45.5 ± 0.5	9	0.47 ± 0.06[d,e]	14
1a/8a	−14.4 ± 0.5[b]	−6.3 ± 0.4	46.9 ± 0.6	11	0.67 ± 0.07[c]	19
1/8	−15.2 ± 0.7[a]	−6.0 ± 0.5	47.0 ± 1.0	7	0.93 ± 0.12[e]	23
1/8a	−18.4 ± 0.7[a,b]	−5.4 ± 0.5	45.4 ± 0.5	13	1.2 ± 0.1[d,c]	17

Pooled data are fitted with a combination of a Boltzmann fit and a linear regression either after normalization to its maximal currents or cell capacitance. Half-maximal activation, slope k, and the reverse potential are calculated from the best fit model. The maximal conductance G_{max} is derived from the current density. All data are represented as mean ± SE. Significance was analyzed by a one-way ANOVA, Bonferroni corrected, [a/a]$p < 0.05$, [a/a]$p < 0.0001$, [b/b]$p < 0.001$, [c/c]$p < 0.01$, [d/d]$p < 0.001$, [e/e]$p < 0.05$.
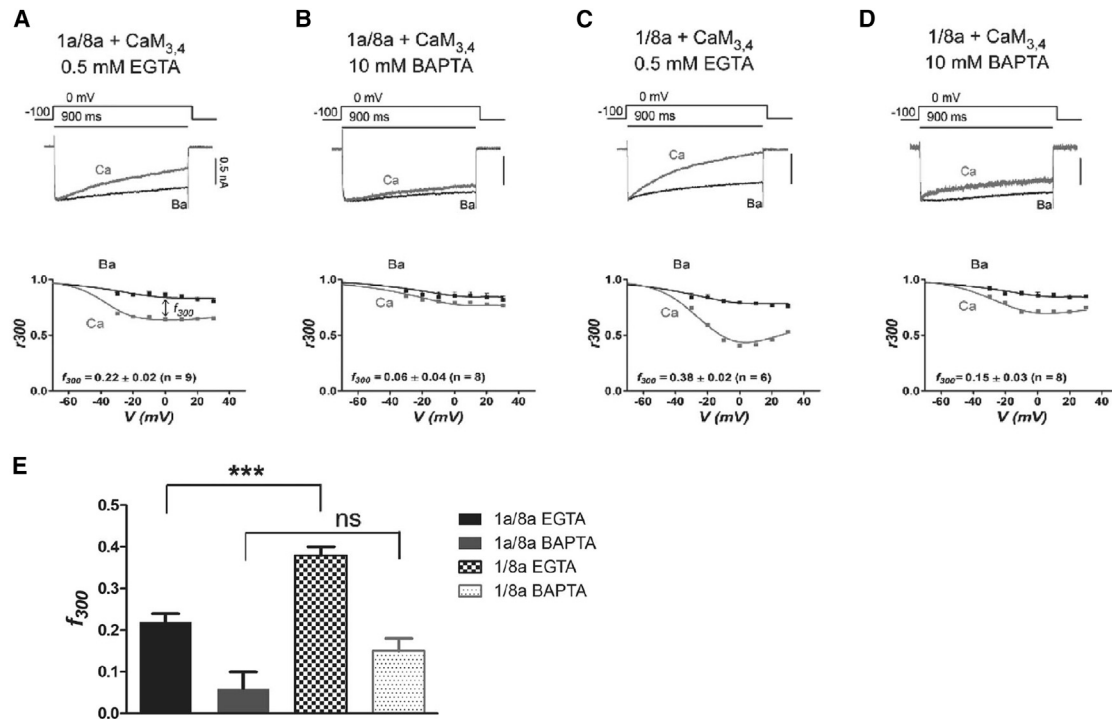
FIGURE 4 Inclusion of alternative exon 1a or 1 influences the extent of *NSCaTE*-mediated Ca^{2+}-dependent inactivation. (*A*) The splice variant 1a/8a was co-transfected with $CaM_{3,4}$, and the currents were recorded in the presence of low-buffering 0.5 mM EGTA in the internal solution. The top shows example traces in Ca^{2+} (*gray*) and Ba^{2+} (*black*). The current bar refers to the Ba^{2+} trace, and the Ca^{2+} trace is normalized to the Ba^{2+} peak. The bottom gives the average CDI; r_{300} refers to the ratio of current at 300 ms of voltage step as compared to the peak current, and f_{300} to the same at 0 mV. The results are means ± SE; cell numbers are shown in parentheses. (*B*) The results for 1a/8a CDI, high-buffering 10 mM BAPTA, are shown in the same format as in (*A*). (*C*) The results for 1/8a CDI, low-buffering, are shown in the same format as in (*A*). (*D*) The results for 1/8a CDI, high-buffering, are shown in the same format as in (*A*). (*E*) A bar chart reporting the statistics for the f_{300} values is shown. ***$p < 0.001$; ns, nonsignificant as compared to the vector control (Student's unpaired *t*-test).

extent and with a notable and significant change in steady-state activation involving $Ca_V\beta_3$ (Figs. S2 and S3; Tables S2 and S3).

In summary, the observed kinetic effects are most prominent on exon-1-containing $Ca_V1.2$ channels and are, however, to some extent β-subunit-dependent, with $Ca_V\beta_{2a}$ showing a larger effect on steady-state inactivation, whereas $Ca_V\beta_3$ clearly showed a stronger effect on channel activation potentials.

Alternative splicing of N-terminus and domain I of $Ca_V1.2$ did not affect unitary basic gating properties

The macroscopic nature of voltage-gated ion currents (*I*) can be approximately described by $I = n \times i \times f_{active} \times p_{open}$, where *n* represents the "channel number," *i* is the "unitary conductance" of a single ion channel, *f* the channel "availability," and *p* represents the channel's "open probability" (36). An increased current density can be explained either by an elevated number of functional channels or by increased channel open probability. For further evaluation, we investigated whether the increased current density of the 1/8a isoform was due to altered single-channel open

probability (p_{open}) or to an increased number of channels (*n*) inserted in the cell surface membrane. We compared unitary currents of all four isoforms in cell-attached patches, with 110 mM Ba^{2+} in the pipette solution (HP -100 mV, TP $+10$ mV). Fig. 7, *A* and *B* shows 10 consecutive exemplary traces with their respective ensemble average currents of single $Ca_V1.2$ isoforms 1a/8, 1a/8a and 1/8, 1/8a. Basic gating properties such as slow and fast kinetics were not altered by alternative splicing (Table 4). Besides, a quantification of channel open- and closed-state live time did not uncover any alteration in fast $Ca_V1.2$ gating properties (Fig. S4, *A–H*; Table S4). Our conclusion regarding the unaltered single-channel gating properties of all four isoforms suggests that the observed effect in a higher-current density for the exon 1 isoform could be due to a higher channel surface expression.

Larger gating currents of isoform 1 revealed an increase in channel surface expression

Ion channel surface expression can be either determined by a biochemical method or by analyzing the current density based on a gating current analysis (Q_{on}) (49,50). The capacitive voltage-sensor movement of voltage-gated ion
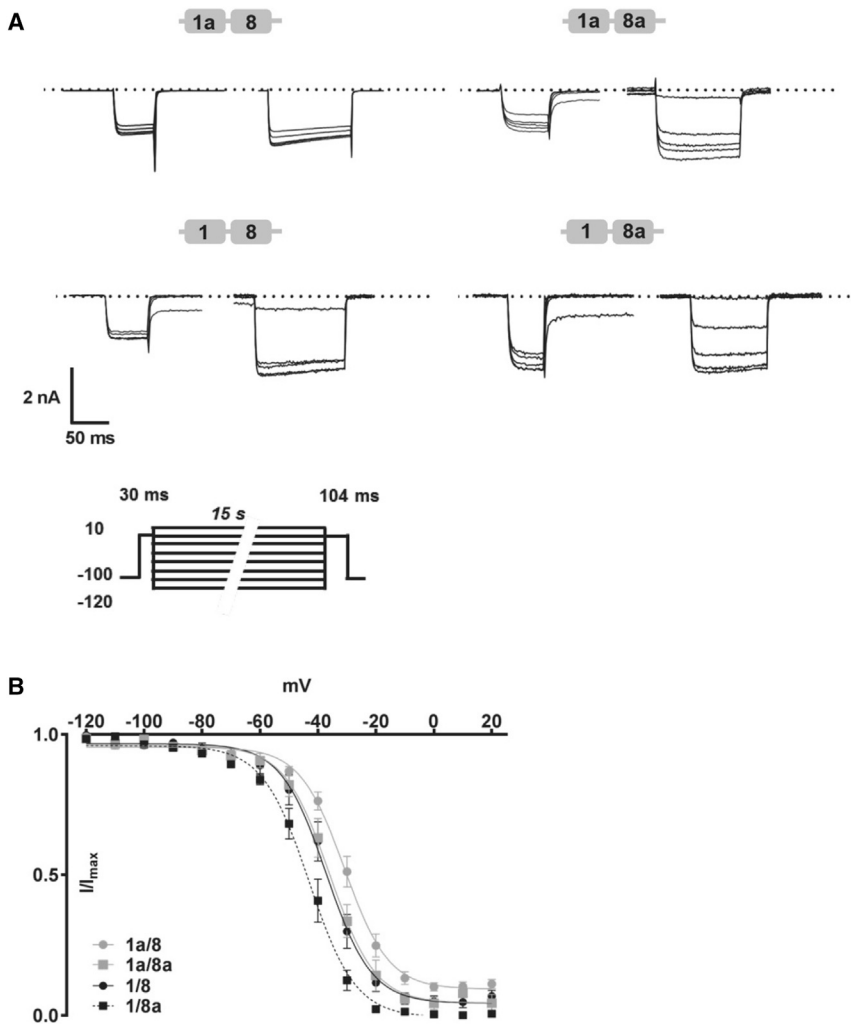
FIGURE 5 Differences in steady-state inactivation of Ca$_V$1.2 isoforms in HEK 293 cells. (*A*) Representative Ba^{2+} traces (5 mM) after 15 s conditioning pulses elicited at TP of -120, -90, -60, -40, or -20 mV are shown. (*B*) The mean ensemble of the steady-state inactivation kinetics is shown. The plots are derived from currents normalized to its maximum and fitted with a single Boltzmann function. Data are presented as mean $\pm$ SE. The kinetic parameters are listed in Table 2.

channels can be observed based on channel activation through various depolarizing potentials, whereas the net ionic inward and outward currents were observed at the reverse potential (E_{rev}). At the reversal potential, no ionic current was present, as the net I$_{Ba}$ was zero, and only the small gating currents remained (Fig. 8 *A*). Fig. 8 *A* (*lower right panel*) shows significantly larger Q_{on} for isoforms containing the exon 1 variant over the exon 1a variant, as shown for 1/8 over 1a/8 and 1/8a over 1a/8a (unpaired *t*-test, *p < 0.05, ***p < 0.001).

We additionally quantified our observed increase in current density (pA/pF) from Fig. 2 *C* by plotting the tails versus the activation potential and normalizing it to the cell capacitance (Fig. 8 *B*). Owing to the inherent property of ion channels to inactivate over time, a tail current protocol was used for a more defined analysis of ion conductance *GV*, as the number of active channels directly correlates with the measured tail currents. Again, isoform 1/8a clearly surpassed all the other isoforms in supporting a very large current density. However, an expected increase in current density was not observed for the 1/8 isoform as it was in

our I-V experiments. Based on our results and with respect to Ca$_V\beta_{2a}$ modulation, we conclude that 1/8a-Ca$_V$1.2 channels are expressed at a higher level on the plasma membrane to produce substantially larger gating currents.

Higher surface expressions of exon-1-containing Ca$_V$1.2 splice variants

To validate the gating current results, we used a biochemical method to detect surface expressions of all the four Ca$_V$1.2 splice variants coexpressed with Ca$_V\beta_{2a}$. The membrane-bound channels were biotinylated, pulled down with NeutrAvidin, and subjected to Western blot analyses to detect Ca$_V$1.2 protein expressions, and we found that exon-1-containing Ca$_V$1.2 channels were expressed $\sim$2-fold higher than exon-1a-containing channels (Fig. 8 *C*).

DISCUSSION

Here, we have demonstrated that alternative splicing of the N-terminus and domain 1 of the Ca$_V$1.2 calcium channel
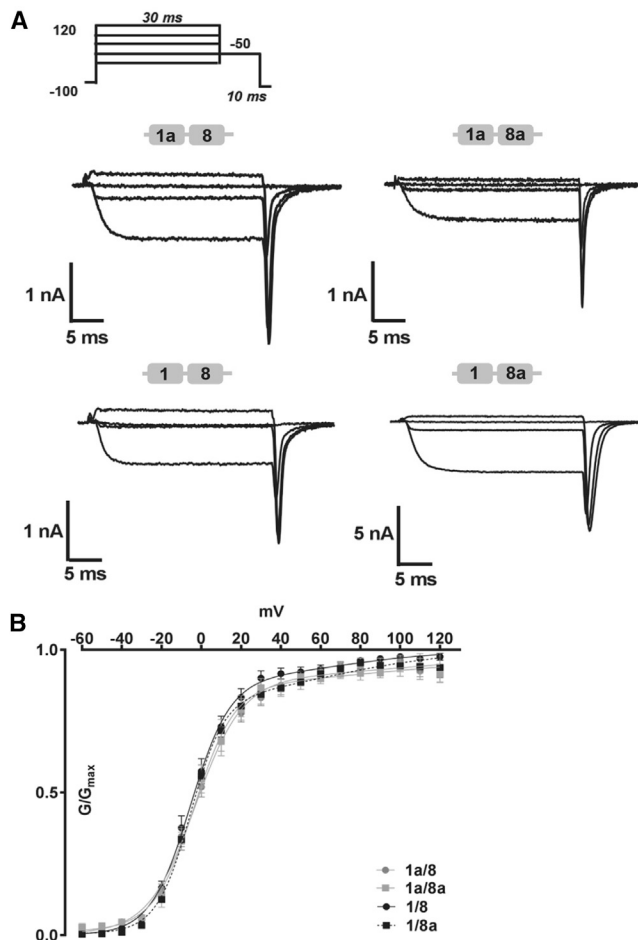
FIGURE 6 Activation kinetics of N-terminal-spliced Ca$_V$1.2 isoforms. (A) Tail currents were evoked by repolarizing pulses of 10 ms at −50 mV after a series of depolarizing TP of −40, 0, 40, or 90 mV. (B) The mean ensemble average of steady-state inactivation kinetics is shown. The plot was fitted with a dual Boltzmann function. Data are presented as mean ± SE. The kinetic parameters are listed in Table 3.

generated different biophysical properties that differ strikingly in channel inactivation and channel surface expression. We compared the predominant human heart isoform 1a/8a/Δ9*/22/32/33 with one human smooth-muscle isoform 1/8/Δ9*/22/32/33 (51). In addition to these isoforms,

TABLE 2 Steady-State Inactivation Currents of Ca$_V$1.2 Obtained in 5 mM Ba^{2+}

Parameters/ Splice Isoform	$V_{1/2inact.}$ (mV)	k	n
1a/8	−30.9 ± 0.7	−7.6 ± 0.6	10
1a/8a	−36.0 ± 0.9[a,c]	−7.8 ± 0.8	10
1/8	−37.2 ± 0.9[b]	−7.8 ± 0.8	11
1/8a	−43.1 ± 0.7[a,b,c]	−8.0 ± 0.7	9

The half-maximal inactivation ($V_{1/2inact.}$) was calculated from the normalized currents after a single Boltzmann fit was applied. The slope factor is given as the k-value, and n represents the number of experiments. Data are given as mean ± SE. Significance testing was done by a one-way ANOVA, Bonferroni corrected, [a/a]$p < 0.01$, [b/b]$p < 0.05$, [c/c]$p < 0.0001$.

**TABLE 3 Steady-state Activation Kinetics of the Four Analyzed Ca$_V$1.2 Isoforms Obtained in 5 mM Ba^{2+}**

Parameters/ Splice Isoform	$V_{1/2act.}$ (mV)	k_{low}	k_{high}	n
1a/8	−3.0 ± 1.0[a]	11.8 ± 1.2	52.6 ± 32.9	15
1a/8a	−3.5 ± 1.1[b]	10.1 ± 1.2	63.1 ± 22.7	11
1/8	−5.5 ± 1.0[a,b,c]	10.0 ± 1.2	28.9 ± 26.1	8
1/8a	−5.5 ± 1.1[c]	8.4 ± 1.5	33.3 ± 14.0	9

Half-maximal activation was determined by a dual Boltzmann function when $G = 0.5G_{max}$. Slope factors (k) are given for the low and high threshold components of the function. All data are represented as mean ± SE. For statistical significance, a one-way ANOVA was applied. Data were Bonferroni corrected, [a/a]$p < 0.001$, [b/b]$p < 0.0001$, [c/c]$p < 0.001$.

we constructed 1/8a/Δ9*/22/32/33, which depicts a subpopulation of 23% in rat hearts (19) and that was reported as the rat brain isoform (45), and 1a/8/Δ9*/22/32/33, which so far has not been reported to our knowledge. Significantly, the 1/8a isoform shows the most distinct difference in gating patterns with respect to voltage-dependent activation and inactivation, N-lobe CDI, and, to a smaller extent, channel activation. On a macroscopic scale, Ba^{2+} and Ca^{2+} currents seemed to be strongly influenced by the choice of exons 1 or 1a. As reported in 2008, Ca^{2+} selectivity of the N-lobe CaM regulation of Ca$_V$1.2 and Ca$_V$1.3 channels is not invariably global but can be switched to local Ca^{2+}-sensing via binding of the N-lobe on a NSCaTE, located within the constitutive exon 2 of the N-terminus of Ca$_V$1.2 (34). Although CDI due a to rise in local Ca^{2+} has been solely attributed to the C-lobe of CaM (46,47) and not to the N-lobe, here we show that on transfection with the mutant CaM$_{3.4}$ and in 0.5 mM EGTA, the N-lobe exerted robust CDI upon 900-ms depolarizing pulses. Of note and in this context, the shorter exon-1-containing Ca$_V$1.2 variants responded with a more robust CDI as compared to the longer exon 1a isoform. This result implies that local Ca^{2+}-sensing N-lobe modulation of brain and smooth-muscle exon-1-containing Ca$_V$1.2, being more robust, will restrict Ca^{2+} entry. Such a customized Ca$_V$1.2 regulation could be beneficial for local Ca^{2+} entry in neuronal cells, whose tight control is vital for long-term synaptic plasticity (52–54), or in cardiac cells for ventricular excitability (55). Interestingly, a human mutation, A39V, has been identified in patients suffering from Brugada syndrome, a cardiac disorder that exhibited Ca$_V$1.2 loss of function resulting in ventricular arrhythmia (56). The alanine at position 39 of 1/8a isoform is 13 amino acids away from W52, which is the tryptophan residue that is critical for CaM binding (57). For the 1a/8a isoform, the critical tryptophan residue (W) is at position 82 (W82) (34). The A39V mutation attenuated N-lobe CDI, in which the f$_{300}$ index, a measure of CDI, is reduced by 50% (58). However, in the report, the "neuronal" isoform of 1/8a was used, and in our results, this isoform produced robust N-lobe CDI as compared to the heart 1a/8a isoform. An

A
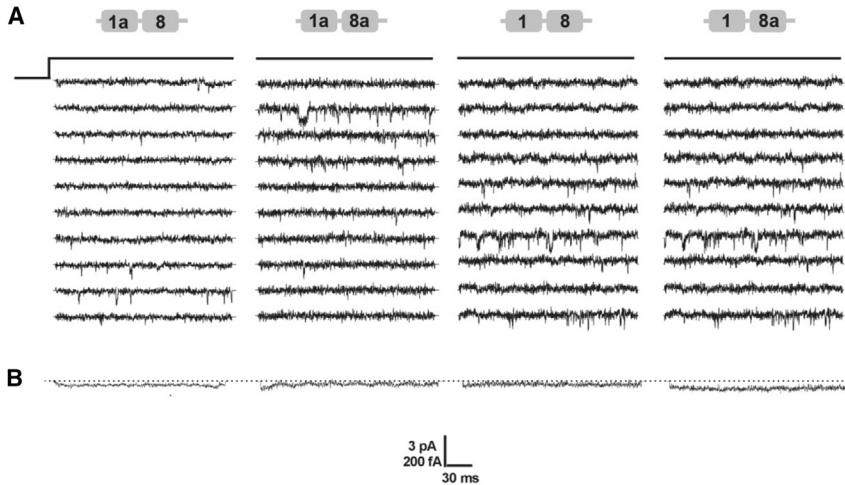
FIGURE 7 Exemplary single-channel traces of recombinant Ca$_V$1.2 calcium channel isoforms. HEK 293 cells were transiently transfected with Cav1.2, $\alpha_2\delta_1$, β_{2a}, and GFP in equal molar ratios. An illustration of the applied pulse protocol (150-ms pulse length, HP of -100 mV, test pulse to $+10$ mV, interpulse time 1 Hz) is shown. (*A*) Ten representative consecutive traces of at least 180 recorded sweeps per experiment are highlighted for each channel isoform. (*B*) The mean ensemble average current derived from 180 traces is shown. Scale bar is given in pA for single-channel events and in fA for averaged traces.

attenuation of N-lobe CDI would have been a rather large gain of function with regards to the 1/8a variant. However, we speculate that if the 1a/8a isoform were characterized, the gain of function would have been modest, and as such, the A39V main loss-of-function effect could primarily have arisen from lower surface expression of the mutant channels (56), as the surface expression of the 1/8a-A39V mutant channels was similar to wild-type (59). Taken together, this may explain the seeming lack of overt neurological phenotype in Brugada patients.

Besides CaM binding to the N-terminus of Ca$_V$1.2, calcium-binding protein (CaBP1) also binds to a region more distal to the CaM binding site to influence function (60,61). CaMKII that has been reported to be tethered to the N-terminus of Ca$_V$1.2 is likely to work in tandem with CaM binding to W52 (62). However, discovering how alternative splicing of the N-terminus may affect all these interactions will require future work. For the Ca$_V$2 channels, the N-terminus of Ca$_V$2.1 plays a role in the proper folding of the protein, and the N-terminus of the truncated channel plays a dominant negative role to downregulate the func-

tional channels via the unfolded protein response and endoplasmic-reticulum-associated protein degradation (63,64). However, a native Ca$_V$1.2 N-terminus splice variant that contained exons 1 and 2, because of a premature stop codon just upstream of exon 2, could not exert a dominant effect on N-lobe CDI (34). For the Ca$_V$2.2 channel, three amino acids (S48, R52, and R54) found within the N-terminus are critical for G-protein modulation (65).

Exons 8 and 8a moderated additionally voltage-dependent inactivation and inactivation kinetics. Whole-cell patch-clamp electrophysiological experiments clearly showed that inactivation in all four isoforms was enhanced in correlation with Ca$_V$1.2 molecular identity in the following order in the presence of Ca$_V\beta_{2a}$: 1/8a > 1a/8a > 1/8 > 1a/8 (Table 2). Several direct and indirect mechanisms have been proposed for channel inactivation, with key contributions of the N-terminus of the β-subunit, the IS6, I-II and II-III loops, and the C-terminus of the α1-subunit (66–71). Human mutations in exons 8 and 8a of the *CACNA1C* gene have been associated with the multiorgan disorder Timothy's syndrome (16,72). Although most

TABLE 4 Synopsis of Single-Channel Parameter Derived from HEK 293 Cells Transiently Transfected with Human Ca$_V$1.2 Isoforms $\alpha2\delta1$ and β_{2a}

Parameters/Splice Isoform	1a/8	1a/8a	1/8	1/8a	*p*-value
Availability (%)	68 ± 10 (6)	60 ± 7 (9)	61 ± 9 (8)	52 ± 11 (5)	$p > 0.05$
P_{open} (%)	4.1 ± 0.7 (6)	3.0 ± 0.5 (9)	6.0 ± 0.7 (8)	4.2 ± 0.8 (5)	$p > 0.05$
$I_{unitary}$ (pA)	0.82 ± 0.04 (6)	0.88 ± 0.03 (9)	0.78 ± 0.04 (8)	0.79 ± 0.03 (5)	$p > 0.05$
I_{peak} (fA)	48 ± 9 (6)	48 ± 8 (9)	46 ± 9 (8)	53 ± 16 (5)	$p > 0.05$
Mean open time (ms)	0.44 ± 0.04 (6)	0.35 ± 0.04 (8)	0.35 ± 0.04 (8)	0.36 ± 0.05 (5)	$p > 0.05$
τ_{open} (ms)	0.32 ± 0.03(6)	0.29 ± 0.03(8)	0.29 ± 0.03(8)	0.31 ± 0.04 (5)	$p > 0.05$
Mean close time (ms)	9.3 ± 2.7 (6)	5.6 ± 1.4 (6)	5.6 ± 1.4 (6)	4.7 ± 1.9 (5)	$p > 0.05$

Unitary events were recorded with a 110-mM intracellular barium solution from cells held at a holding potential (HP) of -100 mV and pulsed to $+10$ mV for 150 ms. Parameters were idealized after semiautomatic leak subtraction with pClamp10. Mean open time and mean close time are given as arithmetic mean values. Tau values for mean close time could not be determined because of a too-small number of real single-channel events ($n = 1$). The fraction of active sweeps (availability) and open probability (P_{open}) were corrected according to the channel number (n). $I_{unitary}$ was analyzed by visual estimation. The local extreme of the maximal peak (I_{peak}) was derived from mean-ensemble average currents (>180 sweeps) after smoothening. The recorded cell number is given in parenthesis. Parameters are given as mean ± SE. A one-way ANOVA was used to determine statistical significance with a 0.05% confidence interval, $p > 0.05$.

A

B

C
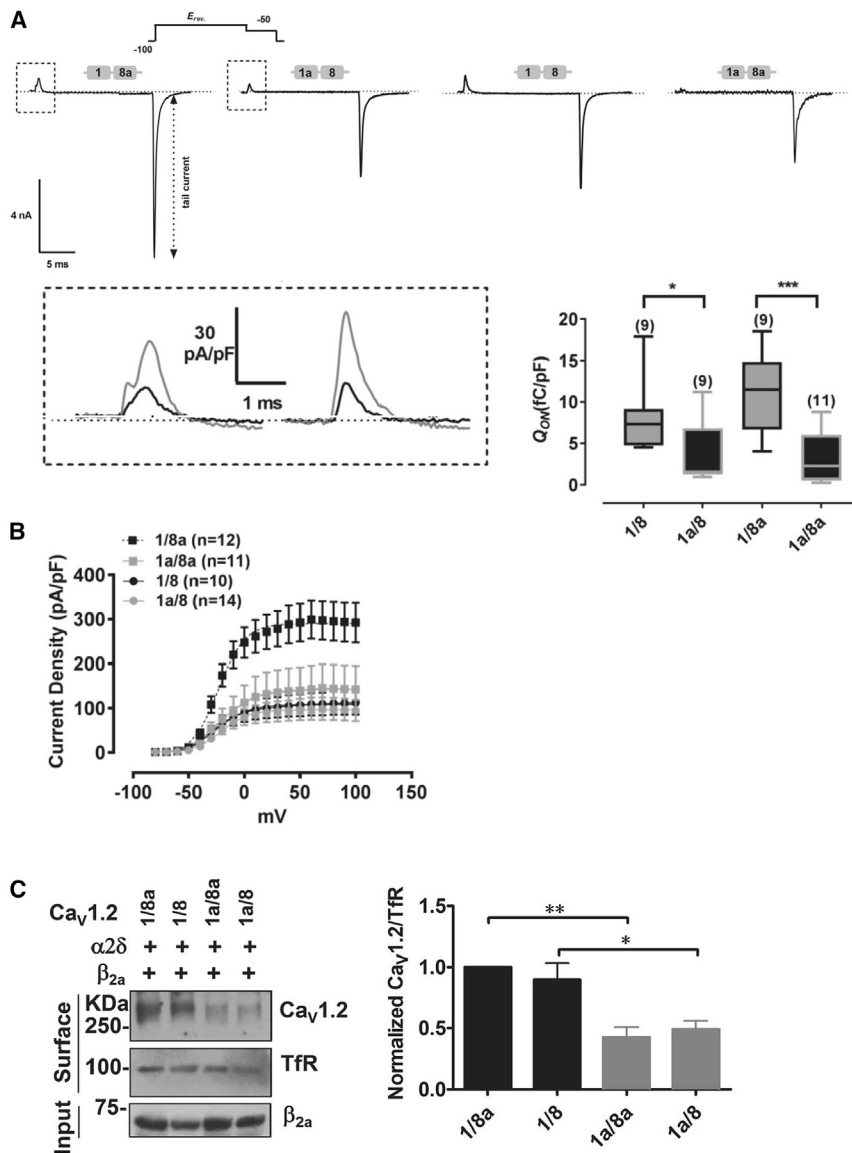
FIGURE 8 Quantification of surface expressions of $Ca_V1.2$ splice variants. (*A*) The Q_{on} measured by tail protocol from HEK 293 cells transfected with $Ca_V1.2$ calcium channel isoforms is shown. Representative traces (*top panel*) of step depolarizations to the reversal potential (E_{rev}) were elicited for 20 ms with a subsequent hyperpolarizing pulse of -50 mV for 10 ms, during which the gating current was measured. The movement of the total charge, ON-gating (Q_{on}), during depolarization, was recorded in 5-mM Ba^{2+}. A magnification of exemplary Q_{on} currents (*bottom*, *left panel*) for isoforms 1/8a_1a/8 (*left*) and 1/8_1a/8a (*right*) is shown. Q_{on} was normalized to its capacitance (pF). A box-plot for ON-gating currents is given (*bottom*, *left panel*). Data show median, 25, and 75% percentiles, minimum and maximum. An unpaired *t*-test was used for significance testing, *$p < 0.05$, **$p < 0.01$. (*B*) The *GV* relationship obtained from tail currents that were normalized to their cell capacitance is shown. (*C*) The surface protein levels of N-terminal $Ca_V1.2$ splice variants in transfected HEK 293 cells are shown. Representative western blot and quantifications of biotinylated surface 1/8a, 1/8, 1a/8a, and 1a/8 isoforms overexpressed in HEK 293 cells are shown ($n = 4$; *left panel*). An unpaired *t*-test was used for significance testing, *$p < 0.05$ and $p** < 0.01$ (population data; *right panel*).

patients die of cardiac arrhythmia, they also display neurological disorders such as autism. In line with our findings, it should be worthwhile to characterize these mutations in the context of the combinatorial splicing patterns of the $Ca_V1.2$ channels as identified in various cell types that critically contribute to phenotype (73).

We further analyzed the splicing-dependent gating properties on a microscopic scale by using single-channel recordings. The basic gating properties of unitary $Ca_V1.2$ isoforms remained remarkably constant with regard to slow and fast channel kinetics and with no significant differences, particularly in channel open probability, availability, and unitary current amplitude. This finding, however, was in good agreement in the $Ca_V1.2$ channel splice variant surface expression that we confirmed by quantification of surface protein levels and gating charges Q_{on} on the membrane. Previous studies by our group revealed that the 1/8a isoform

represents a small subpopulation of $Ca_V1.2$ channels in the heart of Wistar-Kyoto rats, and this isoform could be the predominant isoform in the human brain.

The physiological implications for the larger 1/8a-Cav1.2 cell surface expression and current density could be addressed via genetic targeting, such as replacing exon 8a with exon 8 to produce only the 1/8 genotype. In 2007, a novel N-terminal splice variant exon 1c was reported, and this variant was found to be abundantly expressed in rat myogenic arteries and to a lesser extent in cardiac muscles. Interestingly, exon 1c is expressed in rats but not in humans or mice. A comparison of the 1c isoform with the shorter exon 1 isoform revealed a significant difference in channel activation/inactivation property and in Ca^{2+}-dependent regulation in a β-subunit-dependent manner when evaluated in cerebral arteries. Auxiliary $Ca_V1.2$ subunits, such as the β- or $\alpha_2\delta$-subunit, are known to be involved in channel

trafficking via interaction with the endoplasmic reticulum retention or exit signals. However, although the idea is widely accepted that the N-terminus of Ca$_V$1.2 is essential for plasma membrane trafficking and that this regulation is subject to β-subunit regulation, a thorough investigation using various human β-subunit isoforms β_1, β_{2a}, β_3, and β_4 in combination with the Ca$_V$1.2 1/1a/1c isoforms is lacking.

In summary, we directly compared the functional differences between the human Ca$_V$1.2 1/1a and 8/8a isoforms at a macroscopic and microscopic level and found that the N-terminal length decoded by exon 1 affects channel inactivation and surface expression. Further work will be required to determine whether various auxiliary subunits and/or phosphorylation by protein kinase A and/or C could further expand on the diversity of Ca$_V$1.2 function to customize to a specific physiological response or pathological condition.

SUPPORTING MATERIAL

Four figures and four tables are available at http://www.biophysj.org/biophysj/supplemental/S0006-3495(18)30399-0.

ACKNOWLEDGMENTS

REFERENCES

1. Reuter, H. 1979. Properties of two inward membrane currents in the heart. *Annu. Rev. Physiol.* 41:413–424.

2. Tsien, R. W. 1983. Calcium channels in excitable cell membranes. *Annu. Rev. Physiol.* 45:341–358.

3. Sinnegger-Brauns, M. J., A. Hetzenauer, …, J. Striessnig. 2004. Isoform-specific regulation of mood behavior and pancreatic beta cell and cardiovascular function by L-type Ca 2+ channels. *J. Clin. Invest.* 113:1430–1439.

4. Deisseroth, K., E. K. Heist, and R. W. Tsien. 1998. Translocation of calmodulin to the nucleus supports CREB phosphorylation in hippocampal neurons. *Nature.* 392:198–202.

5. Dolmetsch, R. E., U. Pajvani, …, M. E. Greenberg. 2001. Signaling to the nucleus by an L-type calcium channel-calmodulin complex through the MAP kinase pathway. *Science.* 294:333–339.

6. Langwieser, N., C. J. Christel, …, S. Moosmang. 2010. Homeostatic switch in hebbian plasticity and fear learning after sustained loss of Cav1.2 calcium channels. *J. Neurosci.* 30:8367–8375.

7. Zamponi, G. W., J. Striessnig, …, A. C. Dolphin. 2015. The physiology, pathology, and pharmacology of voltage-gated calcium channels and their future therapeutic potential. *Pharmacol. Rev.* 67:821–870.

8. Dolphin, A. C. 2016. Voltage-gated calcium channels and their auxiliary subunits: physiology and pathophysiology and pharmacology. *J. Physiol.* 594:5369–5390.

9. Dolphin, A. C. 1999. L-type calcium channel modulation. *Adv. Second Messenger Phosphoprotein Res.* 33:153–177.

10. Hullin, R., I. F. Khan, …, S. Herzig. 2003. Cardiac L-type calcium channel beta-subunits expressed in human heart have differential effects on single channel characteristics. *J. Biol. Chem.* 278:21623–21630.

11. Dolphin, A. C. 2003. Beta subunits of voltage-gated calcium channels. *J. Bioenerg. Biomembr.* 35:599–620.

12. Arikkath, J., and K. P. Campbell. 2003. Auxiliary subunits: essential components of the voltage-gated calcium channel complex. *Curr. Opin. Neurobiol.* 13:298–307.

13. Hu, Z., M. C. Liang, and T. W. Soong. 2017. Alternative splicing of L-type Ca$_V$1.2 calcium channels: implications in cardiovascular diseases. *Genes (Basel).* 8:E344.

14. Li, G., J. Wang, …, T. W. Soong. 2017. Exclusion of alternative exon 33 of Ca$_V$1.2 calcium channels in heart is proarrhythmogenic. *Proc. Natl. Acad. Sci. USA.* 114:E4288–E4295.

15. Abernethy, D. R., and N. M. Soldatov. 2002. Structure-functional diversity of human L-type Ca2+ channel: perspectives for new pharmacological targets. *J. Pharmacol. Exp. Ther.* 300:724–728.

16. Splawski, I., K. W. Timothy, …, M. T. Keating. 2004. Ca(V)1.2 calcium channel dysfunction causes a multisystem disorder including arrhythmia and autism. *Cell.* 119:19–31.

17. Gidh-Jain, M., B. Huang, …, N. el-Sherif. 1995. Reemergence of the fetal pattern of L-type calcium channel gene expression in non infarcted myocardium during left ventricular remodeling. *Biochem. Biophys. Res. Commun.* 216:892–897.

18. Jurkat-Rott, K., and F. Lehmann-Horn. 2004. The impact of splice isoforms on voltage-gated calcium channel alpha1 subunits. *J. Physiol.* 554:609–619.

19. Tang, Z. Z., X. Hong, …, T. W. Soong. 2007. Signature combinatorial splicing profiles of rat cardiac- and smooth-muscle Cav1.2 channels with distinct biophysical properties. *Cell Calcium.* 41:417–428.

20. Tang, Z. Z., M. C. Liang, …, T. W. Soong. 2004. Transcript scanning reveals novel and extensive splice variations in human l-type voltage-gated calcium channel, Cav1.2 alpha1 subunit. *J. Biol. Chem.* 279:44335–44343.

21. Liao, P., T. F. Yong, …, T. W. Soong. 2005. Splicing for alternative structures of Cav1.2 Ca2+ channels in cardiac and smooth muscles. *Cardiovasc. Res.* 68:197–203.

22. Soldatov, N. M. 1994. Genomic structure of human L-type Ca2+ channel. *Genomics.* 22:77–87.

23. Soldatov, N. M. 1992. Molecular diversity of L-type Ca2+ channel transcripts in human fibroblasts. *Proc. Natl. Acad. Sci. USA.* 89:4628–4632.

24. Hofmann, F., V. Flockerzi, …, J. W. Wegener. 2014. L-type Ca$_V$1.2 calcium channels: from in vitro findings to in vivo function. *Physiol. Rev.* 94:303–326.

25. Liao, P., D. Yu, …, T. W. Soong. 2007. A smooth muscle Cav1.2 calcium channel splice variant underlies hyperpolarized window current and enhanced state-dependent inhibition by nifedipine. *J. Biol. Chem.* 282:35133–35142.

26. Welling, A., A. Ludwig, …, F. Hofmann. 1997. Alternatively spliced IS6 segments of the alpha 1C gene determine the tissue-specific dihydropyridine sensitivity of cardiac and vascular smooth muscle L-type Ca2+ channels. *Circ. Res.* 81:526–532.

27. Tang, Z. Z., P. Liao, …, T. W. Soong. 2008. Differential splicing patterns of L-type calcium channel Cav1.2 subunit in hearts of spontaneously hypertensive rats and Wistar Kyoto rats. *Biochim. Biophys. Acta.* 1783:118–130.

28. Liao, P., G. Li, …, T. W. Soong. 2009. Molecular alteration of Ca(v)1.2 calcium channel in chronic myocardial infarction. *Pflugers Arch.* 458:701–711.

29. Wang, J., S. S. Thio, …, T. W. Soong. 2011. Splice variant specific modulation of CaV1.2 calcium channel by galectin-1 regulates arterial constriction. *Circ. Res.* 109:1250–1258.

30. Shistik, E., T. Ivanina, …, N. Dascal. 1998. Crucial role of N terminus in function of cardiac L-type Ca2+ channel and its modulation by protein kinase C. *J. Biol. Chem.* 273:17901–17909.

31. Cheng, X., J. Liu, …, J. H. Jaggar. 2007. A novel Ca(V)1.2 N terminus expressed in smooth muscle cells of resistance size arteries modifies channel regulation by auxiliary subunits. *J. Biol. Chem.* 282:29211–29221.

32. Bannister, J. P., C. M. Thomas-Gatewood, …, J. H. Jaggar. 2011. Ca(V) 1.2 channel N-terminal splice variants modulate functional surface expression in resistance size artery smooth muscle cells. *J. Biol. Chem.* 286:15058–15066.

33. Bannister, J. P., S. Bulley, …, J. H. Jaggar. 2016. Rab25 influences functional Cav1.2 channel surface expression in arterial smooth muscle cells. *Am. J. Physiol. Cell Physiol.* 310:C885–C893.

34. Dick, I. E., M. R. Tadross, …, D. T. Yue. 2008. A modular switch for spatial Ca2+ selectivity in the calmodulin regulation of CaV channels. *Nature.* 451:830–834.

35. Sachs, F., J. Neil, and N. Barkakati. 1982. The automated analysis of data from single ionic channels. *Pflugers Arch.* 395:331–340.

36. Schröder, F., and S. Herzig. 1999. Effects of beta2-adrenergic stimulation on single-channel gating of rat cardiac L-type Ca2+ channels. *Am. J. Physiol.* 276:H834–H843.

37. Bartels, P., K. Behnke, …, S. Herzig. 2009. Structural and biophysical determinants of single Ca(V)3.1 and Ca(V)3.2 T-type calcium channel inhibition by N(2)O. *Cell Calcium.* 46:293–302.

38. Sigworth, F. J., and S. M. Sine. 1987. Data transformations for improved display and fitting of single-channel dwell time histograms. *Biophys. J.* 52:1047–1054.

39. Pang, L., G. Koren, …, S. Nattel. 2003. Tissue-specific expression of two human Ca(v)1.2 isoforms under the control of distinct 5′ flanking regulatory elements. *FEBS Lett.* 546:349–354.

40. Saada, N. I., E. D. Carrillo, …, P. Palade. 2005. Expression of multiple CaV1.2 transcripts in rat tissues mediated by different promoters. *Cell Calcium.* 37:301–309.

41. Biel, M., P. Ruth, …, F. Hofmann. 1990. Primary structure and functional expression of a high voltage activated calcium channel from rabbit lung. *FEBS Lett.* 269:409–412.

42. Cheng, X., J. Pachuau, …, J. H. Jaggar. 2009. Alternative splicing of Cav1.2 channel exons in smooth muscle cells of resistance-size arteries generates currents with unique electrophysiological properties. *Am. J. Physiol. Heart Circ. Physiol.* 297:H680–H688.

43. Benmocha, A., L. Almagor, …, N. Dascal. 2009. Characterization of the calmodulin-binding site in the N terminus of CaV1.2. *Channels (Austin).* 3:337–342.

44. Zühlke, R. D., A. Bouron, …, H. Reuter. 1998. Ca2+ channel sensitivity towards the blocker isradipine is affected by alternative splicing of the human alpha1C subunit gene. *FEBS Lett.* 427:220–224.

45. Snutch, T. P., W. J. Tomlinson, …, M. M. Gilbert. 1991. Distinct calcium channels are generated by alternative splicing and are differentially expressed in the mammalian CNS. *Neuron.* 7:45–57.

46. Liang, H., C. D. DeMaria, …, D. T. Yue. 2003. Unified mechanisms of Ca2+ regulation across the Ca2+ channel family. *Neuron.* 39:951–960.

47. Peterson, B. Z., C. D. DeMaria, …, D. T. Yue. 1999. Calmodulin is the Ca2+ sensor for Ca2+ -dependent inactivation of L-type calcium channels. *Neuron.* 22:549–558.

48. DeMaria, C. D., T. W. Soong, …, D. T. Yue. 2001. Calmodulin bifurcates the local Ca2+ signal that modulates P/Q-type Ca2+ channels. *Nature.* 411:484–489.

49. Armstrong, C. M., and F. Bezanilla. 1973. Currents related to movement of the gating particles of the sodium channels. *Nature.* 242:459–461.

50. Baig, S. M., A. Koschak, …, H. J. Bolz. 2011. Loss of Ca(v)1.3 (CACNA1D) function in a human channelopathy with bradycardia and congenital deafness. *Nat. Neurosci.* 14:77–84.

51. Liao, P., D. Yu, …, T. W. Soong. 2004. Smooth muscle-selective alternatively spliced exon generates functional variation in Cav1.2 calcium channels. *J. Biol. Chem.* 279:50329–50335.

52. Moosmang, S., N. Haider, …, T. Kleppisch. 2005. Role of hippocampal Cav1.2 Ca2+ channels in NMDA receptor-independent synaptic plasticity and spatial memory. *J. Neurosci.* 25:9883–9892.

53. Oliveira, A. M., and H. Bading. 2011. Calcium signaling in cognition and aging-dependent cognitive decline. *Biofactors.* 37:168–174.

54. Toescu, E. C., and A. Verkhratsky. 2007. The importance of being subtle: small changes in calcium homeostasis control cognitive decline in normal aging. *Aging Cell.* 6:267–273.

55. Alseikhan, B. A., C. D. DeMaria, …, D. T. Yue. 2002. Engineered calmodulins reveal the unexpected eminence of Ca2+ channel inactivation in controlling heart excitation. *Proc. Natl. Acad. Sci. USA.* 99:17185–17190.

56. Antzelevitch, C., G. D. Pollevick, …, C. Wolpert. 2007. Loss-of-function mutations in the cardiac calcium channel underlie a new clinical entity characterized by ST-segment elevation, short QT intervals, and sudden cardiac death. *Circulation.* 115:442–449.

57. Simms, B. A., I. A. Souza, and G. W. Zamponi. 2014. A novel calmodulin site in the Cav1.2 N-terminus regulates calcium-dependent inactivation. *Pflugers Arch.* 466:1793–1803.

58. Simms, B. A., I. A. Souza, and G. W. Zamponi. 2014. Effect of the Brugada syndrome mutation A39V on calmodulin regulation of Cav1.2 channels. *Mol. Brain.* 7:34.

59. Simms, B. A., and G. W. Zamponi. 2012. The Brugada syndrome mutation A39V does not affect surface expression of neuronal rat Cav1.2 channels. *Mol. Brain.* 5:9.

60. Findeisen, F., and D. L. Minor, Jr. 2010. Structural basis for the differential effects of CaBP1 and calmodulin on Ca(V)1.2 calcium-dependent inactivation. *Structure.* 18:1617–1631.

61. Zhou, H., K. Yu, …, A. Lee. 2005. Molecular mechanism for divergent regulation of Cav1.2 Ca2+ channels by calmodulin and Ca2+-binding protein-1. *J. Biol. Chem.* 280:29612–29619.

62. Hudmon, A., H. Schulman, …, G. S. Pitt. 2005. CaMKII tethers to L-type Ca2+ channels, establishing a local and dedicated integrator of Ca2+ signals for facilitation. *J. Cell Biol.* 171:537–547.

63. Page, K. M., F. Heblich, …, A. C. Dolphin. 2004. Dominant-negative calcium channel suppression by truncated constructs involves a kinase implicated in the unfolded protein response. *J. Neurosci.* 24:5400–5409.

64. Mezghrani, A., A. Monteil, …, P. Lory. 2008. A destructive interaction mechanism accounts for dominant-negative effects of misfolded mutants of voltage-gated calcium channels. *J. Neurosci.* 28:4501–4511.

65. Cantí, C., K. M. Page, …, A. C. Dolphin. 1999. Identification of residues in the N terminus of alpha1B critical for inhibition of the voltage-dependent calcium channel by Gbeta gamma. *J. Neurosci.* 19:6855–6864.

66. Chien, A. J., X. Zhao, …, M. M. Hosey. 1995. Roles of a membrane-localized beta subunit in the formation and targeting of functional L-type Ca2+ channels. *J. Biol. Chem.* 270:30036–30044.

67. Stotz, S. C., and G. W. Zamponi. 2001. Structural determinants of fast inactivation of high voltage-activated Ca(2+) channels. *Trends Neurosci.* 24:176–181.

68. Zhang, J. F., P. T. Ellinor, …, R. W. Tsien. 1994. Molecular determinants of voltage-dependent inactivation in calcium channels. *Nature.* 372:97–100.

69. Shi, C., and N. M. Soldatov. 2002. Molecular determinants of voltage-dependent slow inactivation of the Ca2+ channel. *J. Biol. Chem.* 277:6813–6821.

70. Soldatov, N. M., M. Oz, …, M. Morad. 1998. Molecular determinants of L-type Ca2+ channel inactivation. Segment exchange analysis of the carboxyl-terminal cytoplasmic motif encoded by exons 40-42 of the human alpha1C subunit gene. *J. Biol. Chem.* 273:957–963.

71. Soldatov, N. M., R. D. Zühlke, …, H. Reuter. 1997. Molecular structures involved in L-type calcium channel inactivation. Role of the carboxyl-terminal region encoded by exons 40-42 in alpha1C subunit in the kinetics and Ca2+ dependence of inactivation. *J. Biol. Chem.* 272:3560–3566.

72. Splawski, I., K. W. Timothy, …, M. T. Keating. 2005. Severe arrhythmia disorder caused by cardiac L-type calcium channel mutations. *Proc. Natl. Acad. Sci. USA.* 102:8089–8096, discussion 8086–8088.

73. Dick, I. E., R. Joshi-Mukherjee, …, D. T. Yue. 2016. Arrhythmogenesis in Timothy Syndrome is associated with defects in Ca(2+)-dependent inactivation. *Nat. Commun.* 7:10370.

Supplemental Information

Alternative Splicing at N Terminus and Domain I Modulates Ca$_V$1.2 Inactivation and Surface Expression

Peter Bartels, Dejie Yu, Hua Huang, Zhenyu Hu, Stefan Herzig, and Tuck Wah Soong

SUPPLEMENTARY

Figure S1 Current-Voltage (IV) relationships of N-terminal spliced $Ca_V1.2$ isoforms determined by electrophysiological recordings in 5 mM Ba^{2+} in the presence of $Ca_V\beta_3$. (*A*) Ensemble of normalized current–voltage relationships of N-terminal spliced isoforms. (*B*) The IV relationships were fitted with a modified Boltzmann-Ohm function. Currents were elicited over various TPs for 900 ms. (*C*) Current densities were normalized to the cell capacitance (pA/pF). Number of recorded cells and kinetic constants are tabulated in Table S1.

Table S1 Current-voltage IV relationship of $Ca_V1.2$ isoforms under 5 mM Ba^{2+} in the presence of $Ca_V\beta_3$. Pooled data are fitted with a combination of a Boltzmann fit and a linear regression either after normalization to its maximum currents or cell capacitance. Half-maximal activation, slope *k* and the reverse potential is calculated from the best fit model. The maximal conductance G_{max} is derived from the current density. All data are represented as mean±SEM. *** P < 0.001 and ns, no significance as compared to 1a/8.

Figure S2 Differences in steady-state inactivation of $Ca_V1.2$ isoforms in HEK 293 cells. (*A*) Mean ensemble of the steady-state inactivation kinetics. The plots are derived from currents normalized to its maximum and fitted with a single Boltzmann function. Data are presented as mean ± SEM. The kinetic parameters are listed in Table S2.

Table S2 Steady-state inactivation currents evoked under 5 mM Ba^{2+}. The half-maximal inactivation ($V_{1/2inact.}$) was calculated from the normalized currents after a single Boltzmann fit was applied. The slope factor is given as the *k* value and *n* represents the number of experiments. All data are represented as mean±SEM. *** P < 0.001 and ns, nonsignificant as compared to 1a/8.

Figure S3 Differences in steady-state activation of $Ca_V1.2$ isoforms in HEK 293 cells. (*A*) Mean ensemble of the steady-state inactivation kinetics. The plots are derived from currents normalized to its maximum and fitted with a single Boltzmann function. Data are presented as mean ± SEM. The kinetic parameters are listed in Table S3.

Table S3 Steady-state activation kinetics of the four analysed Cav1.2 isoforms. Half-maximal activation was determined by a dual Boltzmann function when $G = 0.5G_{max}$. Slope factors *(k)* are given for the low and high threshold components of the function. All data are represented as mean ± SEM. ns, no significance, *** P < 0.001 and ** P < 0.01 as compared to 1a/8.

Figure S4 Representative dwell-time histograms obtained from single-channel traces of $Ca_V1.2$ isoforms recorded under 110 mM Ba^{2+}. Open (*A, B, E* and *F*) and close time histograms (*C, D, G* and *H*) were lin-log binned with the Square-Root Method and fitted accordingly to the number of located exponentials with the mean-simplex method (1).

Table S4 Representative tau values obtained from dwell-time histograms shown in Supplementary S1. Tau values are presented with standard error.

Supplementary Reference

1.   McManus, O. B., A. L. Blatz, and K. L. Magleby. 1987. Sampling, log binning, fitting, and plotting durations of open and shut intervals from single channels and the effects of noise. Pflugers Archiv : European journal of physiology 410:530-553.

Figure S1
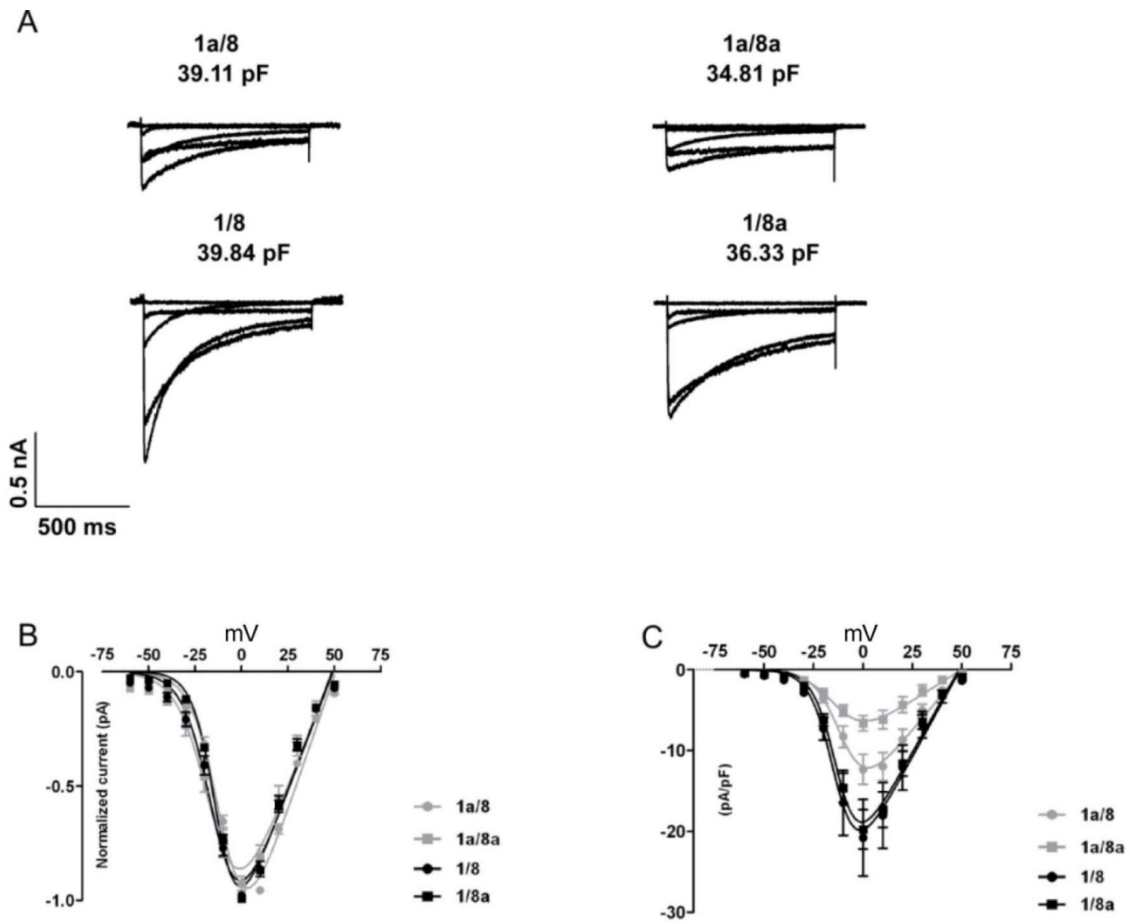
Table S1 Current-voltage IV relationship of $Ca_V1.2$ isoforms plus beta3 obtained in 5 mM Ba^{2+}.

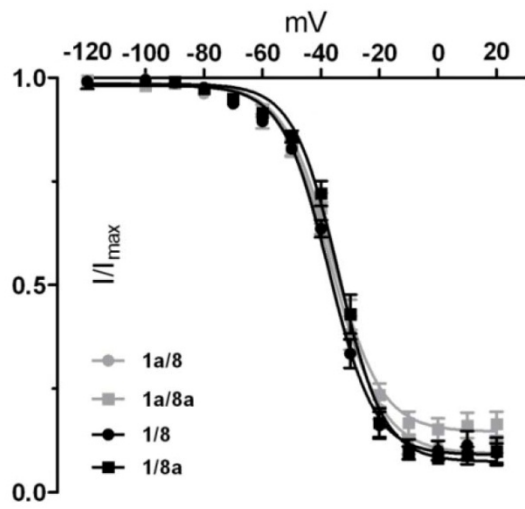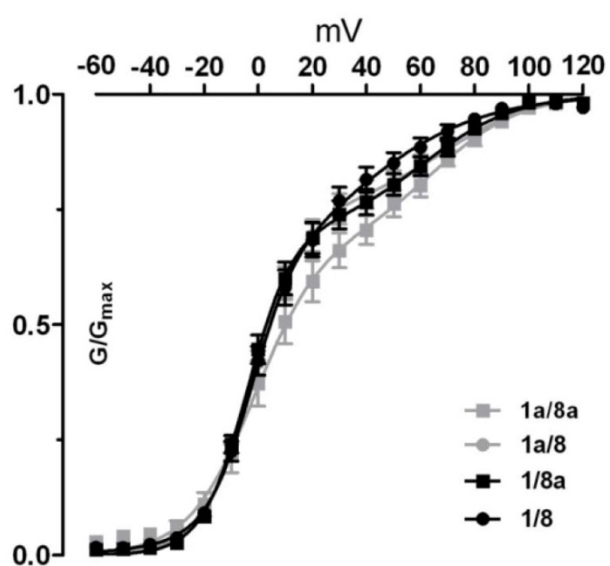| Parameters/ Splice Isoform	$V_{1/2}$ (mV)	k	E_{rev} (mV)	n	G_{max} (pA/pF)	n
1a/8	-9.5±0.7	-7.5±0.4	50.6±0.8	16	0.29±0.03	16
1a/8a	-14.5±1.5[***]	-8.5±0.9[***]	49.6±1.6[*]	13	0.16±0.02[***]	13
1/8	-13.6±0.8[***]	-7.6±0.5[ns]	49.1±1.0[***]	19	0.45±0.07[***]	19
1/8a	-12.4±0.4[***]	-6.1±0.3[***]	48.8±0.6[***]	22	0.43±0.4[***]	22

Figure S2

Table S2 Steady-state inactivation currents of $Ca_V1.2$ plus beta3 obtained in 5 mM Ba^{2+}.

| Parameters/ Splice Isoform	$V_{1/2inact.}$ (mV)	k	n
1a/8	-36.23±0.7	-8.7±0.6	14
1a/8a	-36.0±0.8	-8.4±0.7***	11
1/8	-37.4±0.6***	-7.9±0.5***	10
1/8a	-34.0±0.6***	-7.7±0.5***	10

Figure S3

Table S3 Steady-state activation kinetics of the four analysed $Ca_V1.2$ isoforms plus beta3 obtained in 5 mM Ba^{2+}.

Parameters/ Splice Isoform	$V_{1/2act.}$ (mV)	k_{low}	k_{high}	n
1a/8	-1.6±1.2	9.6±0.8	16.6±4.3	15
1a/8a	-1.4±3.0^{ns}	12.2±1.7***	15.9±4.9^{ns}	16
1/8	-2.7±1.3***	8.1±1.7***	23.6±2.6***	18
1/8a	-4.0±1.1***	8.4±0.8**	16.6±3.6^{ns}	18

Figure S4
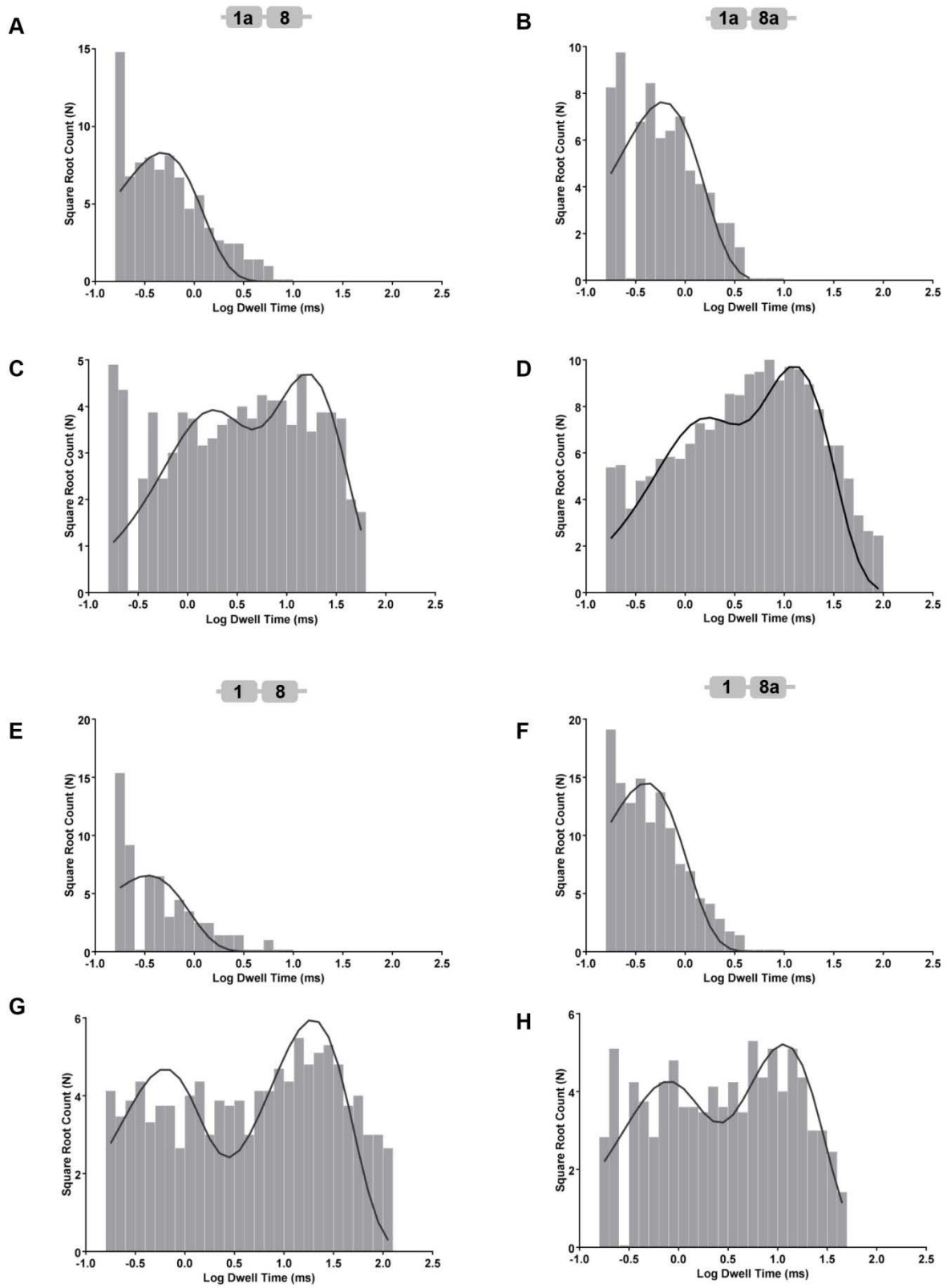
Table S4: Representative tau values obtained from dwell-time histograms shown in Supplementary S4

Splice Isoform/ Parameters	1a/8	1a/8a	1/8	1/8a
τ_{open} (ms)	0.48±0.17	0.54±0.19	0.34±0.29	0.41±0.1
$\tau_{close\,fast}$ (ms)	0.56±0.14	0.63±0.17	1.27±0.25	1.05±0.17
Fraction $_{fast}$	41%	40%	38%	34%
$\tau_{close\,slow}$ (ms)	19.5±0.09	11.5±0.11	16.0±0.15	12.6±0.08
Fraction $_{slow}$	59%	60%	62%	66%